Mechanical stability of the cell nucleus: roles played by the cytoskeleton in nuclear deformation and strain recovery

Xian Wang, [1,2] Haijiao Liu, [1,2] Min Zhu, [1,3] Changhong Cao, [1] Zhensong Xu, [1] Yonit Tsatskis, [4] Kimberly Lau, [3] Chikin Kuok, [4] Tobin Filleter, [1] Helen McNeill, [4,*] Craig A. Simmons, [1,2,*] Sevan Hopyan, [3,5,*] Yu Sun[1,2,*]

[1]Department of Mechanical and Industrial Engineering, University of Toronto, Toronto, Ontario, Canada M5S 3G8; [2]Institute of Biomaterials and Biomedical, University of Toronto, Toronto, Ontario, Canada M5S 3G9; [3]Program in Developmental and Stem Cell Biology, Research Institute, The Hospital for Sick Children, Toronto, Ontario, Canada M5G 1X8; [4]Lunenfeld-Tanenbaum Research Institute, Mt. Sinai Hospital, Toronto, Ontario, Canada M5G 1X5; and [5]Division of Orthopaedic Surgery, Hospital for Sick Children and University of Toronto, Toronto, Ontario, Canada M5G 1X8.

Correspondence and requests for materials should be addressed to sun@mie.utoronto.ca.

Key words: nuclear mechanics, viscoelasticity, cytoskeleton, strain recovery, AFM

Summary statement: Viscoelastic parameters of the cell membrane, cytoskeleton, and nucleus are decoupled, and the roles played by cytoskeleton in maintaining nuclear mechanical stability are deciphered.

Abstract

Extracellular forces transmitted through the cytoskeleton can deform the cell nucleus. Large nuclear deformation increases the risk of disrupting the nuclear envelope's integrity and causing DNA damage. Mechanical stability of the nucleus defines its capability of maintaining nuclear shape by minimizing nuclear deformation and recovering strain when deformed. Understanding the deformation and recovery behavior of the nucleus requires characterization of nuclear viscoelastic properties. Here, we quantified the decoupled viscoelastic parameters of the cell membrane, cytoskeleton, and the nucleus. The results indicate that the cytoskeleton enhances nuclear mechanical stability by lowering the effective deformability of the nucleus while maintaining nuclear sensitivity to mechanical stimuli. Additionally, the cytoskeleton decreases the strain energy release rate of the nucleus and might thus prevent shape change-induced structural damage to chromatin.

Introduction

Extracellular forces can deform the cell nucleus via the cytoskeleton that transmits forces from the cell membrane to the nuclear envelope (Haase et al. 2015). Large nuclear deformation could cause localized loss of nuclear envelope integrity, leading to uncontrolled exchange of nucleo-cytoplasmic contents, DNA damage and cell death (Denais et al 2016). The ability of the nucleus to avoid extreme deformation and extreme strain energy release rate is important for its mechanical stability (Rowat et al. 2006). Quantitative measurements of nuclear deformation and recovery are important for understanding how the nucleus responds to forces and maintains nuclear mechanical stability.

Existing methods for studying nuclear mechanics include micropipette aspiration (Pajerowski et al. 2007), atomic force microscopy (AFM) indentation (Ivanovska et al. 2017), magnetic tweezers (Guilluy et al. 2014), optical tweezers (Schreiner et al. 2015), substrate strain testing (Lombardi et al. 2011), and microfluidic approaches (Hanson et al. 2015). However, the majority of measurements have been made on isolated nuclei or indirectly induce large deformations on a cell to probe the cell nuclear properties (Table SI). We previously used a sharp AFM probe to penetrate the cell membrane to directly measure elasticity of nuclei (Liu et al. 2014). However, the elasticity alone is insufficient to describe nuclear deformation behavior. The viscoelastic properties of the cytoskeleton and the nucleus greatly impact nuclear deformation and strain recovery by dissipating strain energy stored in the deformation (Corbin et al. 2016).

Here, to characterize the viscoelastic properties of the intact nuclei, the nucleus is directly loaded by an AFM probe (Fig. 1A, B) at varying speeds. The AFM probe first deforms and penetrates the cell membrane (Section A in Fig. 1C), then loads the nucleus until penetration of the nuclear envelope (Section B in Fig. 1C). The probe position was recorded by conducting AFM measurement and confocal Z-stack scanning simultaneously (Fig. 1D, Fig. S1). The force-displacement data collected at varied loading speeds were used to quantify the viscoelastic parameters of the cell membrane, cytoskeleton, and nucleus by fitting the data into viscoelastic models. The results revealed that the cytoskeleton stiffens the nucleus through linkage to the nucleus; and the nucleus has inherent capabilities of rapidly releasing the strain energy stored under deformation while the cytoskeleton slows down this high strain energy release rate to protect chromatin structures.

Results

Quantification of elastic modulus and viscosity of the cell membrane, cytoskeleton, and nucleus

When extracellular forces deform the cell membrane, they are transmitted to the nucleus through the cytoskeleton (Fig. 2A). Fig. 2B shows the mechanical model we proposed, where the cell membrane, cytoskeleton, and nucleus are connected in series with each represented by a spring and a damper in the form of the K-V model. Other models have also been used in previous cell mechanics studies (Swift et al. 2013, and Guilluy et al. 2014); however, as detailed in the Materials and Methods, the K-V model was chosen here for describing AFM indentation on viscoelastic solids. The proposed model describes deformation as a function of both the magnitude and the rate of the force stimulus. Force stimulus rate was varied in force-displacement, from which the elastic portion (spring, rate independent) and the viscous portion (damper, rate dependent) in the model were quantified (Eqn. S (5)).

The cytoskeleton mechanically supports the cell membrane (Fig. 2A). When the cell membrane is deformed by the AFM probe, the cytoskeleton also contributes to the mechanical properties measured on the membrane. Instead of considering the measured results as cell membrane properties alone, the measured data (Section A of Fig. 1C) reflects the combined effect of the cell membrane and the cytoskeleton (reduced elastic modulus and reduced viscosity of cell membrane E^* and η^*) but doesn't contain nuclear effects. As the cytoskeleton is connected to the nucleus through the LINC complex, the measured data when the probe deforms the nucleus (Section B of Fig. 1C) reflects the combined effects (reduced elastic modulus and reduced viscosity of nucleus E^{**} and η^{**}) of the nucleus and the cytoskeleton but does not contain effects from the membrane.

To decouple the properties of the cell membrane, cytoskeleton, and nucleus based on the measured combined effects (E^* and E^{**}, η^*, and η^{**}), we also conducted mechanical measurement on isolated nuclei, reflecting only the properties of the nucleus (E_n and η_n). To quantify elastic modulus and viscosity of the cytoskeleton, the reduced modulus calculated from combined effects of the nucleus and cytoskeleton (E^{**} and η^{**}) was substituted with the elastic modulus and viscosity of the nucleus into the reduce modulus equations (Eqn. S. 10-13). Similarly, the elastic modulus and viscosity of the cell membrane were decoupled from the combined effects of the cell

membrane and cytoskeleton (E^* and η^*) by substituting the elastic modulus and viscosity of the cytoskeleton into the reduced modulus equations. Elastic modulus values were determined to be 2.98±0.04 kPa, 4.28±0.33 kPa, and 2.01±0.10 kPa for the membrane, cytoskeleton, and nucleus, respectively. Viscosity values were 4.10±0.06 kPa, 5.43±0.55 kPa·s, and 0.97±0.08 kPa·s for the membrane, cytoskeleton, and nucleus, respectively. These values fit into the range of other reported measurements (Guilak et al. 2000; Dahl et al. 2005). In the decoupling process, the cytoskeleton was assumed to be homogeneous. In reality, the cortex underlying the cell membrane is rich in actin, and potentially explains the higher elastic modulus and viscosity of the membrane.

A separate experiment with a tipless AFM probe was performed (Fig. 2E), and the results were compared to finite element simulation results. Experimentally, indentation depths of 1 μm, 2 μm, 3 μm with rates of 1 μm/s, 5 μm/s, 10 μm/s were applied without penetrating the cells (n = 10). The probe-cell contact area was recorded for converting the force-displacement curves into the strain-stress curves (Fig. 2F). A 3D multi-layered computational model was constructed (Fig. 2G, Karcher et al. 2003; Lau et al. 2015). The material properties assigned to these three layers were from experimentally determined values (Fig. 2D), and the cell and nucleus geometries were constructed from confocal Z stack reconstruction. The same mechanical loads as experiments were exerted on the cell surface of the model, and strain-stress curves were recorded and compared with those from experiments. The results showed good agreement between model-calculated values and the experimental results both in shape and in values with no significant differences (Fig. 2 H-J, correlation coefficient R>0.9), indicating the validity of the measured and decoupled parameters.

Cytoskeleton stiffens cell nucleus to prevent extreme nuclear deformation.

Among the cell membrane, cytoskeleton, and nucleus, the nucleus exhibited the lowest elastic modulus (2.01±0.10 kPa), implying the nucleus can be easily deformed when standing alone. This low elastic modulus almost doubled (3.81±0.21 kPa) when the nucleus was tethered to the cytoskeleton, implying the cytoskeleton stiffens the nucleus to avoid extreme nuclear deformation under extracellular forces. The cytoskeleton has a high elastic modulus and is connected to the nucleus through nucleo-cytoskeletal coupling. It enhances the mechanical stability of the nucleus via stiffening the nucleus to avoid extreme nuclear deformation. When the actin filaments and microtubules in the cytoskeleton were inhibited by nocodazole and cytochalasin D, we observed

significant decrease in the reduced elastic modulus of the nucleus (Fig. 3A). Anti-cytoskeletal drug treatments did not cause significant changes to the elastic modulus and viscosity of isolated nuclei (Fig. S3 C), suggesting that changes in the cytoskeleton do not significantly affect the decoupled properties of nuclei.

Forces from the extracellular matrix are transmitted through the cytoskeleton and cause nuclear deformation. The cytoskeleton's higher elastic modulus relative to the nucleus facilitates nuclear sensitivity to the force transmitted from the cytoskeleton for causing nuclear deformation. Nuclear deformation could promote the expression of Tenascin C (Chiquet et al. 2009), which is an adhesion-modulating protein inhibiting cellular adhesion to fibronectin, and thereby decrease the force transmitted from the extracellular matrix. For isolated nuclei, forces applied on Nesprin-1 induce Emerin phosphorylation and lamin A/C reinforcement (Guilluy et al. 2014). Strengthening of the lamin network results in the stiffening of isolated nuclei, thereby potentially protecting chromatin from excessive mechanical stress.

Cytoskeleton slows down the strain recovery process of cell nucleus.

When an applied stress is removed, the deformation of the nucleus gradually decreases; the stress on nuclear structures is released; and the strain energy stored in the deformation of the spring is gradually dissipated through the damper (Fig. 2B). The stress-strain relationship during strain recovery is $\varepsilon(t) = \frac{\sigma_0}{E}(1 - e^{-\frac{t}{\eta/E}})$, where $\varepsilon(t)$ is the strain, σ_0 is the maximum stress before the strain recovery, η is the viscosity, and E is the elastic modulus. The ratio of viscosity over elastic modulus (time constant), η/E, determines the speed of the exponential decay of strain. The time constant also describes the strain energy release rate in strain recovery, as strain energy decreases linearly with the square of strain, $U = \frac{1}{2}VE\varepsilon(t)^2$, where U is strain energy, V represents the nucleus' volume. A larger time constant means a longer duration of strain relaxation and a lower strain energy release rate (Vincent 2012).

For an isolated nucleus, strain recovery is rapid as the nucleus behaves mostly elastically with a small time constant (0.48±0.05 s, Fig. 3B), which was also observed in micropipette aspiration and in AFM indentation experiments (Dahl et al. 2005). Because of the high viscosity, the cytoskeleton (time constant: 1.27±0.13 s) requires longer time for strain recovery than the nucleus. Therefore, when the nucleus is tethered by the cytoskeleton, the cytoskeleton significantly slows down the

strain recovery of the nucleus (intact vs. isolated: 0.76±0.02 s vs. 0.48±0.05 s), thus a lower strain energy release rate. A high strain energy release rate (i.e., small time constant) indicates a higher risk of structural damage. During strain recovery, the strain energy stored in the elastic portion (Fig. 2B) is dissipated as shear and crack propagation on the structures (Koop & Lewis 2003), which potentially tear chromatin and chromatin-protein bindings, and trigger epigenetic changes (Miroshnikova et al. 2017). Structurally, the cytoskeleton tethers to the nuclear lamina connected with chromatin. The high viscosity of the cytoskeleton significantly slows down the nuclear strain recovery process and lowers the strain energy release rate, potentially provide cushion effects to stabilize chromatin structure.

Anti-cytoskeletal drug treatments revealed both the redundant and distinct role of actin filaments and microtubules in stiffening nucleus and slows down strain recovery. On one hand, disturbing both actin filaments and microtubules resulted in significant softer nuclei than disturbing only actin filaments or only microtubules (Fig. 3A), suggesting that actin filaments and microtubules both play a role in preventing extreme nuclear deformations. On the other hand, disturbing both actin filaments and microtubules resulted in a similar viscosity value than disturbing either one of them (Fig. 3A). These data prove the necessity of having both actin filaments and microtubules to maintain a high viscosity of the nucleus for slowing down the strain recovery process.

In addition, the SUN domain proteins were knocked down using both siRNA pool and individual siRNA and confirmed by qRT-PCR (Fig. 3C-E and Fig. S2), and the properties of membrane, cytoskeleton, nucleus, and isolated nucleus were measured (Fig. 3E and Fig. S2). After knocking down the SUN proteins, the reduced elastic modulus and reduced viscosity became significantly lower than the control, suggesting the necessity of cytoskeleton-nucleus coupling for the cytoskeleton to stiffen the nucleus, prevent extreme deformations, and slow down strain recovery. It was noticed that the depletion of SUN1 or SUN2 alone had a significant effect on nuclear stiffness, indicating their potential distinct roles in nuclear mechanics (Fig. 3C and 3E).

Late stage cancer cells reveal a lower elastic modulus, viscosity, and time constant.

Late-stage cancer cells are known to have the hallmark of gene instability (Simi et al. 2015). Therefore, we next compared the intact nuclei of early (RT4, Stage I) and late stage (T24, Stage III) human bladder cancer cells. For intact RT4 and T24 cells, T24 nuclei exhibit a lower elastic modulus, lower viscosity, and smaller time constant (Fig. 4A, B). Actin and tubulin staining

confirmed that T24 cells have a significantly lower density of the cytoskeleton, leading to the lower elastic modulus and viscosity of the cytoskeleton (Fig. 4C-F, Kim et al. 2014). After anti-cytoskeletal drug treatment (Cytochalasin D and nocodazole), nuclei's reduced elastic modulus decreased from 4.33±0.36 kPa to 3.45±0.20 kPa, the reduced viscosity decreased from 4.47±0.35 kPa·s to 2.54±0.21 kPa·s, and time constant decreased from 1.35±0.25 s to 0.81±0.40 s. After anti-cytoskeletal drug treatment, RT4 nuclei's reduced elastic modulus and viscosity exhibited no significant difference than those of T24 nuclei (Fig. 4A), suggesting the cytoskeleton difference is responsible for the difference in mechanical properties between RT4 and T24 nuclei. However, we also note that the isolated nuclei of RT4 were significantly stiffer than T24 nuclei, which cannot be explained by cytoskeleton differences. The higher stiffness of isolated nuclei of RT4 vs. T24 could potentially be attributed to the higher density of lamin A/C in RT4 (Fig. 4E, F), which is the major nuclear envelope structural protein (Swift et al. 2013).

Discussion

Our findings indicate that the nucleus is a softer organelle relative to the cytoskeleton and coupling with the stiff cytoskeleton helps nucleus avoid extreme nuclear deformations. Large deformations can impose higher stress onto the nuclear envelope, lamins, chromatin, and other structures inside the nucleus. High stress on the nuclear envelope could induce local rupture and cause uncontrolled material exchanges between intra-nuclear and extra-nuclear environments, and DNA damage (Denais et al. 2016; Irianto et al. 2017). High stress also has the potential to alter the conformation of chromatin, binding between chromatin and transcription factors, and to cause histone modifications (Mattout et al. 2015). Tethering between the cytoskeleton and nucleus may help to lower the risk of genetic instability when an extracellular force is exerted on the cell.

Previous work showed universal abnormalities of actin and microtubules in late-stage cancer cells (Sun et al. 2015; Sakthivel 2016), which are consistent with the differences between RT4 and T24 shown in the present study. The structural differences in cytoskeleton imply distinct mechanical properties in late-stage cancer cells in general although further studies are required for characterizing more types of cancer cells. During metastasis, cancer cells need to travel through confined spaces (Denais et al. 2016) which causes chromatin stretching and DNA damage (Irianto et al. 2017). In this process, the low elastic modulus (thus large deformation) and small time constant (thus high strain energy release rate) of cancer cells could play an instrumental role for

inducing gene mutations, adapting themselves to new microenvironments, and facilitating metastasis (Burrell et al. 2013).

Materials and methods

Cell culture

Human bladder cancer T24 and RT4 cells were obtained from the America Type Culture Collection (ATCC, Manassas, VA). Cells were cultured in ATCC-formulated McCoy's 5A modified medium with 10% FBS and 1% penicillin-streptomycin at 37 °C and 5% CO2. Subculture was conducted before cells reached confluency. Before AFM and confocal experiments, T24 and RT4 cells were passaged and seeded at 2500 cells/cm2 in 35 mm Petri dishes and 35 mm glass bottom dishes (P35G-1.0-20-C, uncoated glass bottom dishes, MatTeck Corporation), respectively, for 24 h.

Nucleus isolation

Human bladder cancer T24 cells were removed from the Petri dish by gently scraping with a cell lifter and transferred to a pre-chilled conical tube after they were rinsed with nuclear extraction buffer (active Motif). The cell suspension was subsequently centrifuged for 5 mins at 500 rpm, and the resulting pellet was resuspended in 1× hypotonic buffer (40010, Nuclear Extract Kit, Active Motif) and incubated cell suspension. The nuclei were then separated from the cellular debris after 30 s centrifugations at 14 000 g at 4 °C. The supernatant (cytoplasmic fraction) was discarded and the pellet (containing nuclei) was then suspended and transferred to a 35 mm Petri dish in complete culture medium for 8 h before the AFM measurements, allowing the nuclei to precipitate and weakly attach to the dish surface.

Drug treatment

Cells were treated with either cytochalasin-D (0.2 µg/mL in cell medium, C8273, Sigma-Aldridge) or nocodazole (5 µg/ml in cell medium, M1404, Sigma-Aldridge) to specifically depolymerize actin or tubulin, respectively. The cytochalasin-D powder was firstly resolved in DMSO at concentration of 0.2 mg/mL, and then 1 µL cytochalasin-D solution was added into 1 mL culture medium as the working medium. Similarly, the nocodazole powder was resolved at concentration

of 5 mg/mL in DMSO, and 1 µL nocodazole solution was added into 1 mL culture medium as the working medium. For the double-treatment experiments, in which both drugs were used to treat the cells, both cytochalasin-D powder and nocodazole powder were resolved in DMSO at concentration of 0.2 mg/mL and 5 mg/mL in DMSO. Then, 1 µL of the DMSO solution with both drug resolved were added to the cell. 1 µL DMSO was added to control group to avoid the influence from DMSO. Each working medium was added to the cell 60 min prior to the experiment. For staining, the drug solution was added to the 24-well cell culture plate with coverslip 60 mins prior to fixing.

Individual siRNA and siRNA pool treatment

The siRNA pool is a combination of multiple siRNAs targeting the same gene. The SMARTpool SUN1 siRNA from Daharmacon includes four types of siRNAs targeting SUN1, and the SMARTpool SUN2 siRNA includes four types of siRNAs targeting SUN2. Using the siRNA pool could reduce the off-target effect, but may cause more non-specific transcription decrease of other genes. Individual siRNA is more specific than siRNA pool, but may have more off-target effect than siRNA pool. To ensure sufficient knock down and ensure potential off-target effects or non-specific decrease of other genes not to affect the measured nuclear mechanics, we now used both siRNA pool and individual siRNA to knock down SUN1 and SUN2 proteins, after which the reduced elastic modulus and reduced viscosity of the nucleus were measured.

The siRNAs for SUN1 and SUN2 knockdown were purchased from Dharmacon (human SUN1 SMARTpool siRNA L-025277-00 and individual siRNA J-025277-05, and Human SUN2 SMARTpool siRNA L-009959-01 and individual siRNA J-009959-09). The cells were treated with 10 nM siRNA for 72 hours prior to measurements. ON-TARGETplus Non-targeting siRNA (D-001810-01) from Dharmacon was used in the control group.

Fabrication of sharp AFM probe tips

AFM sharp probe tips were formed by processing standard AFM cantilevers (MLCT-D, Bruker) with a focused ion beam (FIB)-scanning electron microscope (SEM) dual beam system (HITACHI NB5000 FIB-SEM). Individual AFM cantilevers were mounted on the SEM stage with probe tips facing upwards. The AFM pyramidal tips were then milled into sharp cylinders by dual ion beams (beam 25-1-80). The milling process was monitored under SEM imaging. The machining process

typically costs 10 mins/probe. The resulting tips were 120-150 nm in diameter and 3-5 μm in length. AFM cantilevers with a sharp tip were used in characterizing the mechanical properties of the cell membrane, cytoskeleton, and nucleus. Only a small deformation was produced before the rupture of the cell membrane occurred, conforming to the small-strain assumption of the Hertz model in contact mechanics. The tension effect was minimized via the use of sharp AFM tips that produced a small contact area and small indentation depth.

AFM measurement and data analysis

Force-displacement data were collected at room temperature using an AFM (Bioscope Catalyst, Santa Barbara, CA) mounted on a Nikon confocal microscope. Different from the substrate strain test, in which force application is along the cell substrate direction, and micropipette aspiration, in which applied forces are transmitted through a much larger region of cytoskeleton, measurements made in this work were significantly more locally by a sharp AFM probe that applied a normal force perpendicular to cellular structures. Measurement of cells in each petri dish was completed within 20 mins after taken out of incubator. The AFM probes used in experiments were FIB modified as described above, with a nominal spring constant of 0.03 N/m. The spring constant of each probe was calibrated using thermal spectroscopy (Nanoscope 8.10). The loading speeds were set to be 15 μm/s, 30 μm/s, and 45 μm/s, at each of which force-displacement data were collected.

Force-displacement-speed data were measured at the cell center where a distinct separation of plasma membrane and nuclear envelope can be visualized. Data analysis for quantifying reduced modulus from force-indentation-speed data, and decoupling elastic modulus and viscosity from reduced modulus were conducted in MATLAB. The force-displacement data from AFM measurement have a displacement resolution of 0.2 nm and force resolution of 10 pN, capable of capturing the rupture of the cell membrane due to the large force change caused by cell membrane penetration. Force drop after cell membrane penetration is typically larger than 100 pN (Fig. S1 B-D, Bitterli 2012; Obataya et al. 2005; Angle et al. 2014; Liu et al. 2014), and there is also a significant change in the elastic modulus which rules out a mere sudden change of force without cell membrane rupturing. The code of data analysis for rejecting the non-rupture case is available for download at https://github.com/XianShawn/Nuclear_Mechanics.

Viscoelastic model

The viscoelastic model uses springs and dashpots to describe the elastic and viscous properties. The spring-dashpot model provides more information than previous studies on nuclear mechanics, most of which only focused on the elastic property. The model is commonly used for describing viscoelastic properties of cellular structures as it describes both time-variant (the dashpot) and time-invariant (the spring) relationships between stress and strain (Swift et al. 2013, and Guilluy et al. 2014).

Among spring-dashpot models, K-V model, Maxwell model, SLS model are the most commonly used models. The K-V model, where a damper and a spring are connected in parallel, is commonly used to describe the speed-force-deformation behavior of viscoelastic solids. The parallel connection of the spring and the damper separates the force-displacement curve into the speed-invariant portion ($F_{elastic}$) and speed-dependent portion ($F_{viscous}$), namely $F = F_{elastic} + F_{viscous}$. With different indentation speeds of the AFM probe, the speed-invariant portion ($F_{elastic}$) and the speed-dependent portion ($F_{viscous}$) can be separated and analyzed through linear regression (Eq. S7 and Eq. S9) to quantify the elastic modulus E and viscosity η. The Maxwell model, where a damper and a spring are connected in series, is used to describe the relaxation behavior of a material but does not describe creep under indentation (López-Guerra et al. 2014). The AFM technique used in this work is in essence a creep test (indentation). Using the Maxwell model to describe creep under indentation would result in an extremely high viscosity value and an extremely low elastic modulus value since the Maxwell model assumes the material under testing flows and does not reach the steady state in a creep test. The standard linear solid (SLS) model can be used for describing both viscoelastic solids and viscoelastic fluids. However, compared to the K-V model (two components) and the Maxwell model (two components), the SLS model contains three components while AFM speed-force-deformation data does not contain the stress rate ($\dot{\sigma}$) information that is necessary for fitting all the three parameters in the SLS model. Direct fitting speed-force-deformation data from our AFM measurement using the SLS model resulted in a correlation coefficient as low as 0.4±0.2 (based on 30 speed-force-deformation curves captured in experiments). Thus, in this work, the SLS model was not chosen for data analysis.

As nucleus, cytoskeleton, and cell membrane behave more as viscoelastic solids, the K-V model was assumed to describe the speed-force-deformation behavior of the materials. The time constant of the strain recovery process quantitatively describes how fast strain recovery occurs in K-V model. Comparisons made between the group of nucleus only and the group of nucleus coupled with cytoskeleton revealed the role played by cytoskeleton in the strain recovery process.

For a viscoelastic material, stress-strain relation in the K-V model is

$$\sigma = E\varepsilon + \eta\frac{d\varepsilon}{t} \quad \text{S. (1)}$$

where σ is stress, ε is strain, $\frac{d\varepsilon}{t}$ is strain rate, E is the elastic modulus and η is the viscosity of the sample.

In terms of forces, the K-V model combines the elastic portion and the viscous portion as

$$F = F_{elastic} + F_{viscous} \quad \text{S. (2)}$$

The Hertz model for a cylindrical tip (the shape of the fabricated AFM probe tips) was applied to determine $F_{elastic}$, according to[45]

$$F_{elastic} = \frac{4}{3}\frac{E_s}{1-{v_s}^2}R^{\frac{1}{2}}d^{\frac{3}{2}} \quad \text{S. (3)}$$

where E_s is the measured sample elastic modulus, v_s is the Poisson's ratio of the sample, R is the tip radium, and d is the displacement of the tip.

As the mechanical strain is calculated as $\varepsilon = \frac{\Delta l}{l} = \frac{vt}{l}$, then,

$$F_{viscous} = S\sigma_{viscous} = \pi Rd \cdot \eta\frac{d\varepsilon(t)}{t} = \eta\frac{v}{l}\pi Rd \quad \text{S. (4)}$$

where the contact area $S = \pi Rd$, according to the Hertz model.

Combining the elastic portion and the viscous portion in the K-V model, the relationship between force, displacement, and speed is

$$F = F_{elastic} + F_{viscous} = \frac{4}{3}ER^{1/2}d^{3/2} + \eta\frac{v}{l}\pi Rd \quad \text{S. (5)}$$

Determination of reduced elastic modulus and reduced viscosity, E*, η^*, E**, and η^{**}

The cell model proposed in this work (Fig. 2A, B) is based on the K-V model for viscoelastic materials.[46] The cell membrane, cytoskeleton, and nucleus are each represented by a spring and a damper connected in parallel. The cell membrane is supported by the cytoskeleton underneath. When measuring the mechanical properties of the cell membrane by analyzing the force-displacement-speed data, the data reflect the coupled mechanical properties of both the cell

membrane and cytoskeleton. As shown in Fig. 2B, the elastic modulus and viscosity extracted from "Section A" of Fig. 1C were reduced modulus E^* and η^*, which describe the combined material properties of the cell membrane and cytoskeleton. Similarly, the nucleus is tethered by the cytoskeleton. The measured mechanical properties from the force-displacement-speed data reflect the coupled mechanical properties of both nucleus and cytoskeleton. As shown in Fig. 2B, the elastic modulus and viscosity extracted from "Section B" of Fig. 1C were reduced modulus E^{**} and η^{**}, which describe the combined material properties of nucleus and cytoskeleton. Because the tip is sharp and capable of penetrating the cell membrane, distinct separation between the membrane indentation process and the nucleus indentation process was observed. Thus, it was assumed that there is no effect from the nucleus when indenting the cell membrane and there is no effect from the cell membrane when indenting the nucleus.

To determine reduced elastic modulus and reduced viscosity, the AFM raw data were imported into MATLAB. Baseline subtraction and ROI (region of interest) selection were conducted. The ROI for quantifying cell membrane's reduced elastic modulus and the cell nucleus' reduced elastic modulus correspond to "Section A" and "Section B" in Fig. 1 C, respectively. After filtering the high frequency noise and interpolation, differentiation of data was conducted for further regression. Differentiating Eq. S. (5) with respect to d results in

$$\dot{F} = 2E^* R^{1/2} d^{1/2} + \eta \frac{v}{l} \pi R \qquad \text{S. (6)}$$

where E^* linearly relates to $d^{1/2}$ and $\dot{F}$. Based on S. (6), regression gives

$$\dot{F} = k_1 d^{1/2} + b_1 \qquad \text{S. (7)}$$

where k_1 and b_1 are linear regression parameters. Then, the reduced elastic modulus of the cell membrane coupled with cytoskeleton was calculated from regression as

$$E^* = \frac{k_1}{2R^{1/2}} \qquad \text{S. (8)}$$

To calculate the reduced viscosity, ΔF was defined as the force difference between two indentation speeds, namely $\Delta F = F_{v_1} - F_{v_2}$. According to Eq. S. (5),

$$\Delta F = \eta^* \frac{\Delta v}{l} \pi R d \qquad \text{S. (9)}$$

where Δv equals to $v_1 - v_2$, and the reduced viscosity η^* linearly relates to d and ΔF.

Then, the regression function is constructed as,

$$\Delta F = k_2 d + b_2$$

where k_2 and b_2 are linear regression parameters.

The reduced viscosity of the cell membrane coupled with cytoskeleton is

$$\eta^* = \frac{k_2}{\frac{\Delta v}{l}\pi R} \quad \text{S. (10)}$$

The analysis for determining the reduced elastic modulus E^{**} and reduced viscosity η^{**} for cell nucleus coupled with cytoskeleton is the same as the above.

Decoupling elastic modulus and viscosity from reduce modulus and reduced viscosity

The relationship between the reduced elastic modulus and reduce viscosity are

$$\frac{1}{E^*} = \frac{1}{E_\mathrm{m}} + \frac{1}{E_\mathrm{c}} \quad \text{S. (11)}$$

$$\frac{1}{E^{**}} = \frac{-1}{E_\mathrm{c}} + \frac{1}{E_\mathrm{n}} \quad \text{S. (12)}$$

where E^* and E^{**} are the reduced elastic modulus of the cell membrane and nucleus, respectively; E_m, E_c, and E_n are the elastic modulus of the membrane, cytoskeleton, and nucleus, respectively.

$$\frac{1}{\eta^*} = \frac{1}{\eta_\mathrm{m}} + \frac{1}{\eta_\mathrm{c}} \quad \text{S. (13)}$$

$$\frac{1}{\eta^{**}} = \frac{-1}{\eta_\mathrm{c}} + \frac{1}{\eta_\mathrm{n}} \quad \text{S. (14)}$$

where η^* and η^{**} are the reduced viscosity of the cell membrane and nucleus, respectively; and η_m, η_c, and η_n are the viscosity of the membrane, cytoskeleton, and nucleus, respectively.

The reduced elastic modulus E^*, $E^{**}$and reduce viscosity η^* and η^{**} were calculated according to the data analysis procedure described in the above section. The elastic modulus and viscosity of cell nucleus, E_n and η_n were calculated based on the measurement on isolated cell nuclei.

Error propagation

Due to variation across cells and due to measurement errors, the mechanical parameters calculated from experimental data have uncertainties. From data analysis, the standard error of reduced modulus E^*, E^{**}, E_n, η^*, η^{**}, η_n, was quantified via one-way ANOVA. When modulus was decoupled from reduced modulus, the error from reduced modulus would propagate to the decoupled modulus.

According to(Ku 1966), the elastic modulus E_m and E_c were calculated as,

$$E_\mathrm{c} = \frac{E_\mathrm{n}E^{**}}{E^{**}-E_\mathrm{n}} \quad \text{S. (14)}$$

$$E_\mathrm{m} = \frac{E_\mathrm{c}E^*}{E_\mathrm{c}-E^*} \quad \text{S. (15)}$$

Similarly, the viscosity η_{m} and η_c were calculated as,

$$\eta_{\mathrm{c}} = \frac{\eta_{\mathrm{n}}\eta^{**}}{\eta^{**}-\eta_{\mathrm{n}}} \quad \text{S. (16)}$$

$$\eta_{\mathrm{m}} = \frac{\eta_{\mathrm{c}}\eta^{*}}{\eta_{\mathrm{c}}-\eta^{*}} \quad \text{S. (17)}$$

From the above equations, uncertainty (standard error, Se) was calculated as

$$Se(E_{\mathrm{c}}) = \sqrt{(\frac{dE_c}{dE_n}Se(E_{\mathrm{n}}))^2 + (\frac{dE_c}{dE^{**}}Se(E^{**}))^2} \quad \text{S. (18)}$$

$$Se(E_m) = \sqrt{(\frac{dE_m}{dE_{\mathrm{c}}}Se(E_c))^2 + (\frac{dE_m}{dE^{*}}Se(E^{*}))^2} \quad \text{S. (19)}$$

$$Se(\eta_{\mathrm{c}}) = \sqrt{(\frac{d\eta_c}{d\eta_n}Se(\eta_3))^2 + (\frac{d\eta_{\mathrm{c}}}{d\eta^{**}}Se(\eta^{**}))^2} \quad \text{S. (20)}$$

$$Se(\eta_m) = \sqrt{(\frac{d\eta_{\mathrm{m}}}{d\eta_{\mathrm{c}}}Se(\eta_2))^2 + (\frac{d\eta_m}{d\eta^{*}}Se(\eta^{*}))^2} \quad \text{S. (21)}$$

Model validation

Model geometry: a computational model was developed to simulate the application of forces exerted by the tipless AFM probe on the cell structure. The model is composed of three layers including cell membrane, cytoskeleton, and nucleus, reconstructed from confocal imaging. The default mesh size and node number were set to be 46386 and 26931, respectively.

Boundary condition: a zero-displacement boundary condition was imposed at the bottom surface, as in experiments, cells were cultured on a rigid (compared with the mechanical properties of the cell) substrate (a glass slide or petri dish). Adjacent layers were connected, and the cytoskeleton is fixed with cell membrane and nucleus.

Mechanical properties: the mechanical properties of the cell membrane, cytoskeleton, and nucleus from the experimental results were assigned to the computation model. Kevin-Voigt model was used to interpret experimental data.

Experiment: experiments were performed using a tipless AFM probe, with different indentation depths (1 μm, 2 μm, 3 μm) and rates (1 μm/s, 5 μm/s, 10 μm/s). Confocal imaging was performed simultaneously with a rate of 8 f/s recording the probe-cell contact area changes, which were used for calculating stress on the cell membrane.

Applied load: the mechanical loads with identical displacement magnitude and rate as in tipless AFM experiments were applied to the cell structure. The strain-stress relationship on the surface of the cell, and the deformation of the nucleus, were extracted from the computational model and compared with those measured in experiments (indentation depth: 1 μm, 2 μm, 3 μm; rate: 1 μm/s, 5 μm/s, 10 μm/s).

Self-consistency of the computation model: mesh sensitivity was investigated to ensure the independence of the results from the computational mesh size. Three mesh sizes were used. Coarse (default mesh from ANSYS workbench), medium and fine meshes consisting of 86381, 46386 and 20438 nodes were used for comparison. All three meshes resulted in similar solution patterns. The solution patterns did not depend on the patterns of the mesh lines. At all time-points, the maximum differences between three computational meshes were less than 3% for maximum stress on cell surface, less than 5% for maximum deformation of cell in the Z direction. The results proved the self-consistency of the computation model.

Error source: the main error source is the variance across cells, as differences in cell geometries and mechanical properties of cellular structures exist. However, comparisons between different cell types (RT4 and T24) are distinct and significant, compared to the variances within each cell type. Error can also stem from the multiple regression process during data analysis, including data transformation and linear regressions, while this error was accounted for during the calculation of error propagation and included in the final results.

Immunostaining

The plasma membrane of a cell was stained with the CellMask Deep Red stain (C10046, CellMask Membrane Stain, ThermoFisher Scientific), and the cell nucleus was stained with the standard Hoechst dye (33258, Sigma-Aldrich). The working solution with concentration of 10 μg/mL of CellMask and 50 μg/mL of Hoechst was prepared by mixing the two stocking solutions in warm PBS before confocal imaging. The cells were rinsed with PBS and incubated with the stain working solution for 20 mins. Then, after removal of all the staining solution, the cells were rinsed by PBS three times and then the cells were immediately imaged with confocal microscopy in live cell imaging solution (Invitrogen). The AFM probe tips were first treated with plasma activation for 2 min. (3-Aminopropyl) triethoxysilane (APTES; 99%) (Sigma-Aldrich) was diluted to 2% in a

mixture of 95% ethanol and 5% DI water. The AFM probe tips were placed into the APTES solution for 10 min and then rinsed with ethanol, dried with nitrogen, and incubated at 120 °C for 1 h. The Alexa Fluor 555 NHS ester (Invitrogen) was dissolved in DMSO to 100 μg/mL and used immediately. The tips were then placed into the stain solution and incubated for 1 h at room temperature, and then washed with PBS and DI water and dried with nitrogen. In experiments, AFM measurement and cell imaging were performed simultaneously (Fig. 1D).

Staining for actin, microtubules, and nucleus was achieved using phalloidin fluorescent conjugate (A12379, Alexa Fluor 488 Phalloidin, ThermoFisher Scientific), tubulin-RFP (C10503, CellLight Tubulin-RFP, BacMam 2.0, ThermoFisher Scientific), and Hoechst 33258 (94403 Hoechst 33258 solution, Sigma-Aldrich), separately. BacMam 2.0 was added directly to the cells after passage. The concentration of BacMam was determined based on the protocol provided by ThermoFisher Scientific. After 18 hours of incubation, cells were rinsed with PBS and fixed with 4% paraformaldehyde for 15 mins at room temperature. Cell membrane was then permeabilized by 0.05% Triton X-100 in PBS for 15 mins at room temperature. After rinsed by PBS, cells were then treated with phalloidin conjugate for 1 hr. The nuclei were labeled by Hoechst 33258.

Staining for lamin-A/C was achieved using lamin A/C antibody (MA3-1000, 1:200, Lamin A/C Monoclonal Antibody, ThermoFisher Scientific) as primary antibody and anti-mouse secondary antibody (A-21202, 1:1000, Donkey anti-Mouse IgG (H+L) Secondary Antibody, Alexa Fluor 488, ThermoFisher Scientific). The immunofluorescent staining for SUN 1/2 proteins (kind gift from Dr. Didier Hodzic's group) was achieved using primary antibody and secondary antibodies according to Crisp et al. 2006. The immunostaining process is similar to the procedure described for actin staining. In short, cells were fixed, permeabilized, treated with primary antibody, secondary antibody, and DAPI (D1306 DAPI, ThermoFisher Scientific).

Quantitative confocal imaging and image analysis

In the sample preparation for quantitate confocal imaging, the same mounting media, coverslip, and fluorophore were used for RT4 and T24 cells. In the imaging process, targets were first found under bright-field imaging to minimize photo bleaching. Microscope settings (e.g., laser intensity, gain, exposure time, illumination, etc.) were kept the same for acquiring images in RT4 and T24 cells. Image acquisitions were conducted in minimum duration to minimize bleaching, while

avoiding saturations. In image analysis, the normalized intensity for actin and tubulin was quantified by dividing actin or tubulin intensity over chromatin intensity for individual cells.

qRT-PCR for detection of siRNA-induced mRNA silencing

RNA was extracted using RNAeasy Micro Kit (Qiagen, 74004), treated with DNaseI (Thermo, 18068-015) and then reverse-transcribed with SuperScript III (Thermo, 18064) following manufacturers' instructions. qRT-PCR was performed with Power SYBR Green PCR MasterMix (Thermo, 4368706) using CFX384 Touch Real-Time PCR Detection System (Bio-Rad). PCR program is: 95°C 10min, 95°C 30s, 60°C 30s, 72°C 30s for 40 cycles, followed by the default dissociation curve program. GAPDH served as reference gene. Statistical analyses were performed in Prism 6. Primer (F represents Forward, and R represents Reverse):

GAPDH_F: GGAGCGAGATCCCTCCAAAAT

GAPDH_R: GGCTGTTGTCATACTTCTCATGG

SUN1_F: ATGTCCCGCCGTAGTTTGC

SUN1_R: CCGTCGAGTCACAGCATCC

SUN2_F: CCAGTCACCCCGAGTCATC

SUN2_R: ATGCTCTAAGGTAACGGCTGT

Statistical test

The elastic modulus and viscosity of cell membrane, cytoskeleton, and nucleus were reported as mean ± standard error. The standard error for calculated values were quantified base on error propagation. The comparisons of each group were conducted by one way ANOVA and Student-Newman-Keuls test for pairwise comparisons in JMP and the statistical significance in each comparison was evaluated as $p < 0.05$ for significance level.

Code availability

The custom-made code for data analysis was written and run in MATLAB R2013a and is available through https://github.com/XianShawn/Nuclear_Mechanics.git. The code is for the purpose of reproducible research, not for commercial usage.

Acknowledgment

The authors thank K. Fenelon and H. Tao for their helpful suggestions. The authors also thank Dr. Didier Hodzic's from Washington University School of Medicine in St. Louis for providing the SUN protein antibodies.

Competing interests

No competing interests declared.

Funding

This work was supported by the National Sciences and Engineering Research Council of Canada via an NSERC Steacie Memorial Fellowship and the Canada Research Chairs program, and the Canadian Institutes of Health Research [143319 to H. McNeill].

Data availability

The AFM datasets, microscope images are available through the link https://github.com/XianShawn/Nuclear_Mechanics. The other data that support the findings of this study are available from the corresponding author upon reasonable request.

References

Angle, M.R., Wang, A., Thomas, A., Schaefer, A.T. and Melosh, N.A., (2014). Penetration of cell membranes and synthetic lipid bilayers by nanoprobes. *Biophysical journal*, 107(9), pp.2091-2100.

Bitterli, J., (2012). AFM Based Single Cell Microinjection: Technological Developements , Biological Experiments and Biophysical Analysis of Probe Indentation. *PhD thesis*, ÉCOLE POLYTECHNIQUE FÉDÉRALE DE LAUSANNE, Lausanne, Switzerland.

Bonakdar, N., Gerum, R., Kuhn, M., Spörrer, M., Lippert, A., Schneider, W., Aifantis, K.E. and Fabry, B., (2016). Mechanical plasticity of cells. *Nature materials*, 15(10), pp.1090-1094.

Burrell, R.A., McGranahan, N., Bartek, J. and Swanton, C., (2013). The causes and consequences of genetic heterogeneity in cancer evolution. *Nature*, 501(7467), pp.338-345.

Chiquet, M., Gelman, L., Lutz, R. and Maier, S., (2009). From mechanotransduction to extracellular matrix gene expression in fibroblasts. *Biochimica et Biophysica Acta (BBA)-Molecular Cell Research*, 1793(5), pp.911-920

Corbin, E.A., Adeniba, O.O., Ewoldt, R.H. and Bashir, R., (2016). Dynamic mechanical measurement of the viscoelasticity of single adherent cells. *Applied Physics Letters*, 108(9), p.093701.

Crisp, M., Liu, Q., Roux, K., Rattner, J.B., Shanahan, C., Burke, B., Stahl, P.D. and Hodzic, D., (2006). Coupling of the nucleus and cytoplasm: role of the LINC complex. *J Cell Biol*, 172(1), pp.41-53.

Dahl, K. N., Engler, A. J., Pajerowski, J. D., and Discher, D. E. (2005). Power-law rheology of isolated nuclei with deformation mapping of nuclear substructures. *Biophysical journal*, 89(4), 2855-2864.

Denais, C.M., Gilbert, R.M., Isermann, P., McGregor, A.L., te Lindert, M., Weigelin, B., Davidson, P.M., Friedl, P., Wolf, K. and Lammerding, J., (2016). Nuclear envelope rupture and repair during cancer cell migration. *Science*, 352(6283), pp.353-358.

Guilak, F., Tedrow, J.R. and Burgkart, R., (2000). Viscoelastic properties of the cell nucleus. *Biochemical and biophysical research communications*, 269(3), pp.781-786.

Guilluy, C., Osborne, L.D., Van Landeghem, L., Sharek, L., Superfine, R., Garcia-Mata, R. and Burridge, K., (2014). Isolated nuclei adapt to force and reveal a mechanotransduction pathway in the nucleus. *Nature cell biology*, 16(4), pp.376-381

Haase, K., Macadangdang, J.K., Edrington, C.H., Cuerrier, C.M., Hadjiantoniou, S., Harden, J.L., Skerjanc, I.S. and Pelling, A.E., (2016). Extracellular forces cause the nucleus to deform in a highly controlled anisotropic manner. *Scientific reports*, 6, p.21300

Hanson, L., Zhao, W., Lou, H.Y., Lin, Z.C., Lee, S.W., Chowdary, P., Cui, Y. and Cui, B., (2015). Vertical nanopillars for in situ probing of nuclear mechanics in adherent cells. *Nature nanotechnology*, 10(6), pp.554-562.

Harada, T., Swift, J., Irianto, J., Shin, J.W., Spinler, K.R., Athirasala, A., Diegmiller, R., Dingal, P.D.P., Ivanovska, I.L. and Discher, D.E., (2014). Nuclear lamin stiffness is a barrier to 3D migration, but softness can limit survival. *J Cell Biol*, pp.jcb-201308029.

Irianto, J., Xia, Y., Pfeifer, C.R., Athirasala, A., Ji, J., Alvey, C., Tewari, M., Bennett, R.R., Harding, S.M., Liu, A.J. and Greenberg, R.A., (2017). DNA damage follows repair factor depletion and

portends genome variation in cancer cells after pore migration. *Current Biology*, 27(2), pp.210-223.

Karcher, H., Lammerding, J., Huang, H., Lee, R.T., Kamm, R.D. and Kaazempur-Mofrad, M.R., (2003). A three-dimensional viscoelastic model for cell deformation with experimental verification. *Biophysical journal*, 85(5), pp.3336-3349.

Kim, T., Gardel, M.L. and Munro, E., (2014). Determinants of fluidlike behavior and effective viscosity in cross-linked actin networks. *Biophysical journal*, 106(3), pp.526-534.

Koop, B.E. and Lewis, J.L., (2003). A model of fracture testing of soft viscoelastic tissues. *Journal of biomechanics*, 36(4), pp.605-608.

Ku, H.H., (1966). Notes on the Use of Propagation of Error Formulas. *Journal of Research of the National Bureau of Standards*, 79(4), pp.75–79.

Lau, K., Tao, H., Liu, H., Wen, J., Sturgeon, K., Sorfazlian, N., Lazic, S., Burrows, J.T., Wong, M.D., Li, D. and Deimling, S., (2015). Anisotropic stress orients remodelling of mammalian limb bud ectoderm. *Nature cell biology*, 17(5), p.569.

Liu, H., Wen, J., Xiao, Y., Liu, J., Hopyan, S., Radisic, M., Simmons, C.A. and Sun, Y., (2014). In situ mechanical characterization of the cell nucleus by atomic force microscopy. *ACS nano*, 8(4), pp.3821-3828.

Lombardi, M.L., Zwerger, M. and Lammerding, J., (2011). Biophysical assays to probe the mechanical properties of the interphase cell nucleus: substrate strain application and microneedle manipulation. *Journal of visualized experiments: JoVE*, (55).

López-Guerra, E. A., and Solares, S. D. (2014). Modeling viscoelasticity through spring–dashpot models in intermittent-contact atomic force microscopy. *Beilstein journal of nanotechnology*, 5, 2149.

Mattout, A., Cabianca, D.S. and Gasser, S.M., (2015). Chromatin states and nuclear organization in development—a view from the nuclear lamina. *Genome biology*, 16(1), p.174.

Miroshnikova, Y.A., Nava, M.M. and Wickström, S.A., (2017). Emerging roles of mechanical forces in chromatin regulation. *J Cell Sci*, 130(14), pp.2243-2250.

Obataya, I., Nakamura, C., Han, S., Nakamura, N. and Miyake, J., (2005). Nanoscale operation of a living cell using an atomic force microscope with a nanoneedle. *Nano letters*, 5(1), pp.27-30.

Özkaya, N., Leger, D., Goldsheyder, D. and Nordin, M., (2016). Fundamentals of biomechanics: equilibrium, motion, and deformation. Springer.

Pajerowski, J.D., Dahl, K.N., Zhong, F.L., Sammak, P.J. and Discher, D.E., (2007). Physical plasticity of the nucleus in stem cell differentiation. *Proceedings of the National Academy of Sciences*, 104(40), pp.15619-15624.

Rowat, A.C., Lammerding, J. and Ipsen, J.H., (2006). Mechanical properties of the cell nucleus and the effect of emerin deficiency. *Biophysical journal*, 91(12), pp.4649-4664.

Sakthivel, K.M. and Sehgal, P., (2016). A novel role of lamins from genetic disease to cancer biomarkers. *Oncology reviews*, 10(2).

Schreiner, S.M., Koo, P.K., Zhao, Y., Mochrie, S.G. and King, M.C., (2015). The tethering of chromatin to the nuclear envelope supports nuclear mechanics. *Nature communications*, 6, p.7159.

Simi, A.K., Piotrowski, A.S. and Nelson, C.M., (2015). Mechanotransduction, metastasis and genomic instability. In Genomic Instability and Cancer Metastasis (pp. 139-158). Springer International Publishing.

Sun, B.O., Fang, Y., Li, Z., Chen, Z. and Xiang, J., (2015). Role of cellular cytoskeleton in epithelial-mesenchymal transition process during cancer progression. Biomedical reports, 3(5), pp.603-610.

Swift, J., Ivanovska, I. L., Buxboim, A., Harada, T., Dingal, P. D. P., Pinter, J., Pajerowski, J.D., Spinler, K.R., Shin, J.W., Tewari, M. and Rehfeldt, F. (2013). Nuclear lamin-A scales with tissue stiffness and enhances matrix-directed differentiation. *Science*, 341(6149), 1240104.

Vincent, J.F., (2012). Structural biomaterials. Princeton University Press.

Wang, N., Tytell, J.D. and Ingber, D.E., (2009). Mechanotransduction at a distance: mechanically coupling the extracellular matrix with the nucleus. Nature reviews Molecular cell biology, 10(1), pp.75-82.

Figures

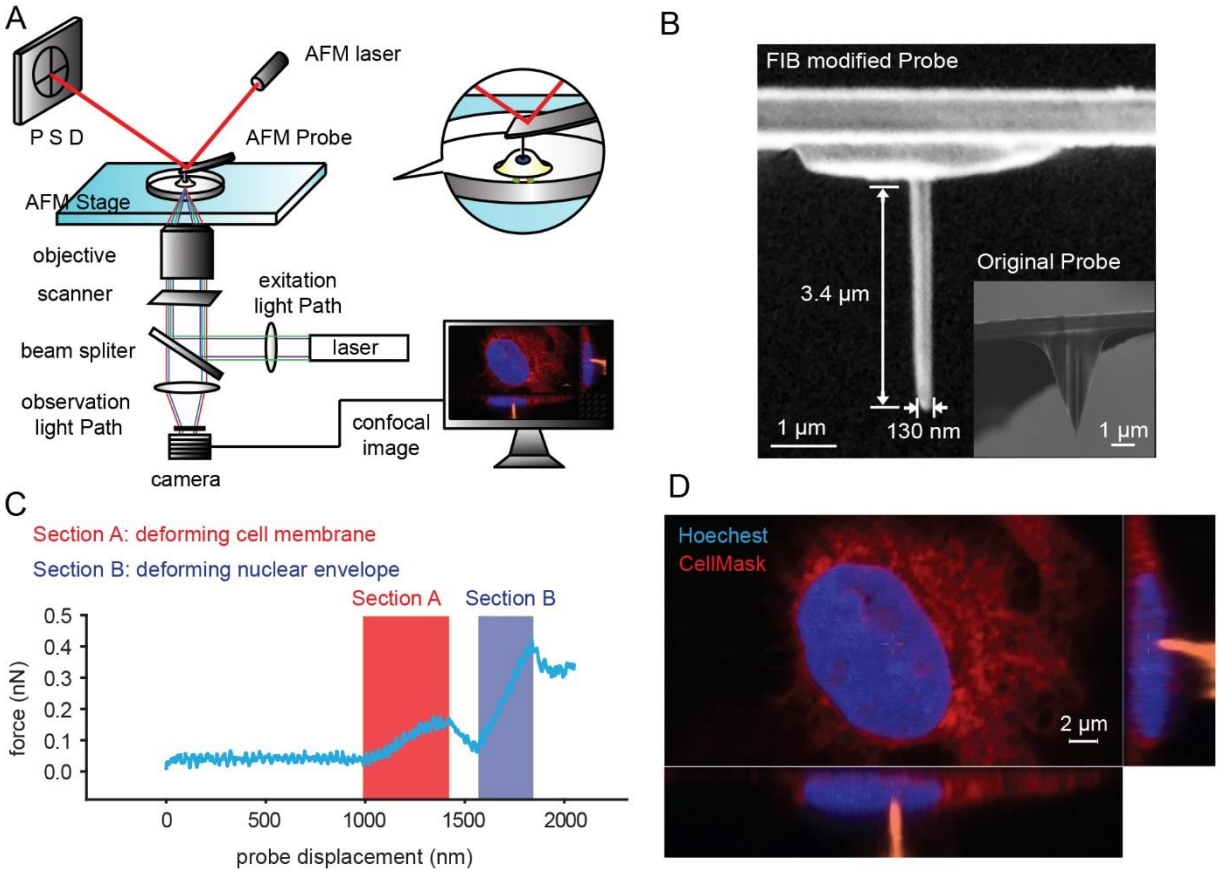

Figure 1. **AFM for measuring cellular and intracellular mechanics.** (A)(B) Focused Ion Beam (FIB)-processed AFM probe enables the penetration of the membrane and nuclear envelope for mechanical measurements. (C) Representative force-displacement data. Force first increases when the probe contacts and loads the membrane until penetration (Section A), after which force decreases until the probe contacts the nuclear envelope when force increases again until the penetrating the nuclear envelope (Section B). (D) AFM probe penetrated both cell membrane and nuclear envelope.

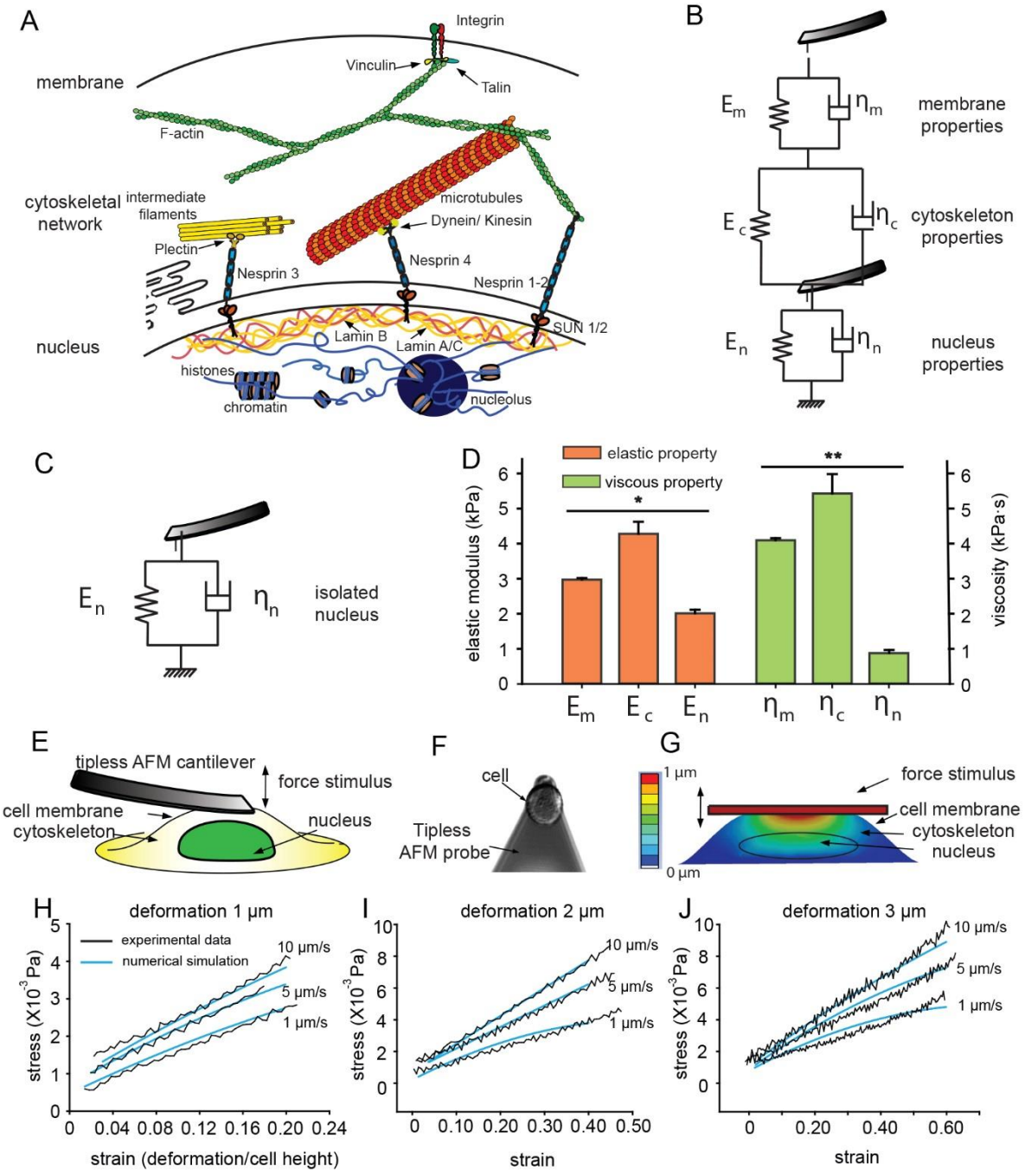

Figure 2. **Viscoelastic properties of the cell membrane, cytoskeleton, and nucleus** (A) Schematic showing the mechanical structures within a cell. (B) Cell mechanics model for interpreting AFM data. (C) Without cytoskeletal effects, the modulus of nucleus was measured by direct measurement on isolated nuclei. (D) Decoupled elastic modulus and viscosity of cell membrane (E_m, η_m), cytoskeleton (E_m, η_c) and nucleus (E_m, η_n) of T24 cells, mean±s.e.m., n $=$ 31, $*P < 1 \times 10^{-10}$, $**P < 1 \times 10^{-14}$. (E) Schematic of validation experiments using a tipless AFM probe. (F) The tipless AFM probe deforms a cell while force-deformation data is recorded. (G) The constructed three-layer computational model. (H-J) Strain-stress curves: comparison between experiments and model-calculated values, with indentation depths of 1 μm (H), 2 μm (I), and 3 μm (J).

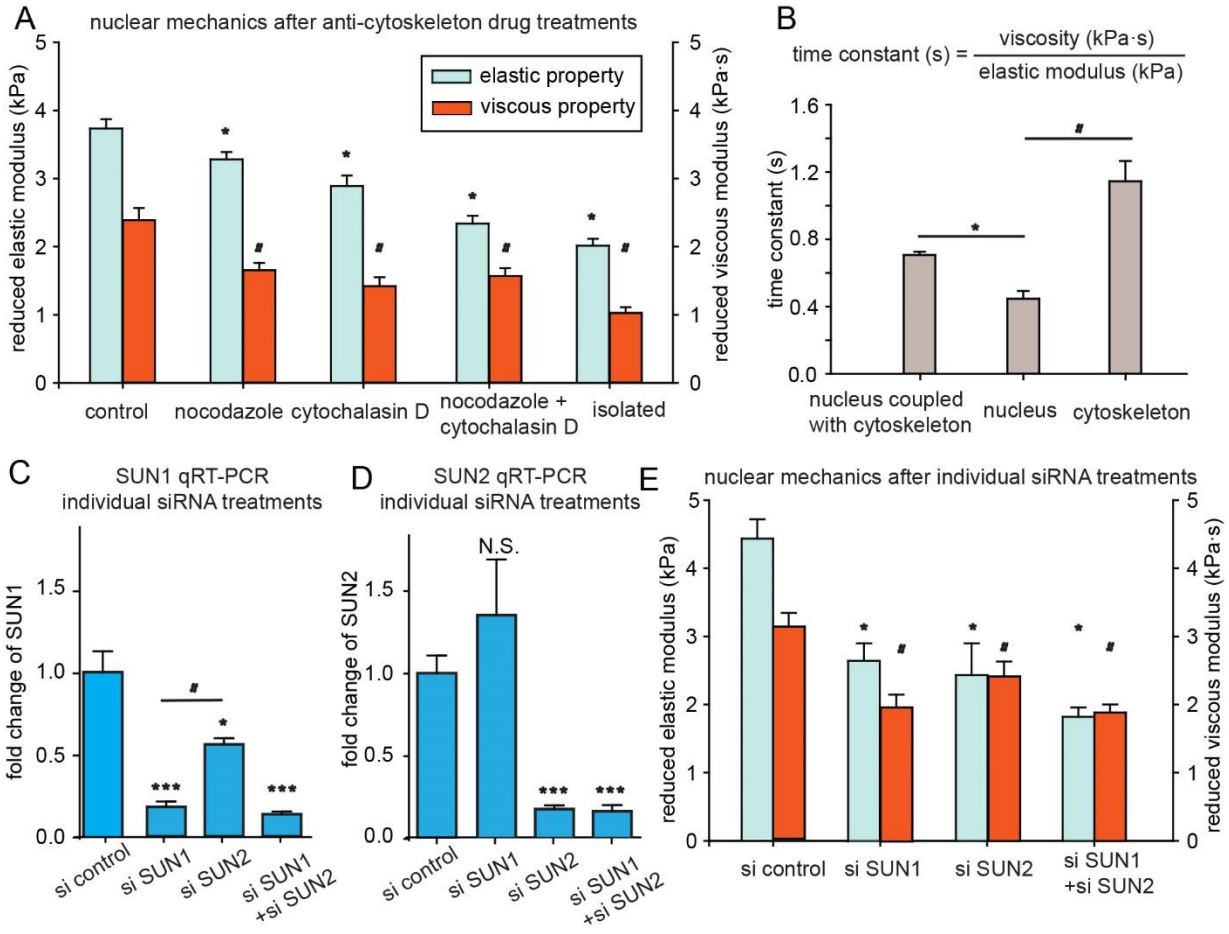

Figure 3. **Nuclear mechanics after drug treatments and SUN protein knockdown.** (A) Experimentally quantified elastic modulus and viscosity, mean±s.e.m., n = 31, *P < 0.01, #P < 0.001 (B) Time constant of nucleus coupled with cytoskeleton, nucleus, and cytoskeleton, mean±s.e.m., n = 31, *P = 3×10^{-6}, #P = 4×10^{-7}. (C)(D) qRT-PCR for individual siRNA knockdown effects for SUN1 (C) and SUN2 (D), n = 4, *P< 0.01, ***P< 0.0001, #P < 0.0001. (E) Reduced modulus and reduced viscosity of nuclei with SUN domain proteins knocked down, mean±s.e.m., n = 15, *P < 0.02, #P < 0.005.

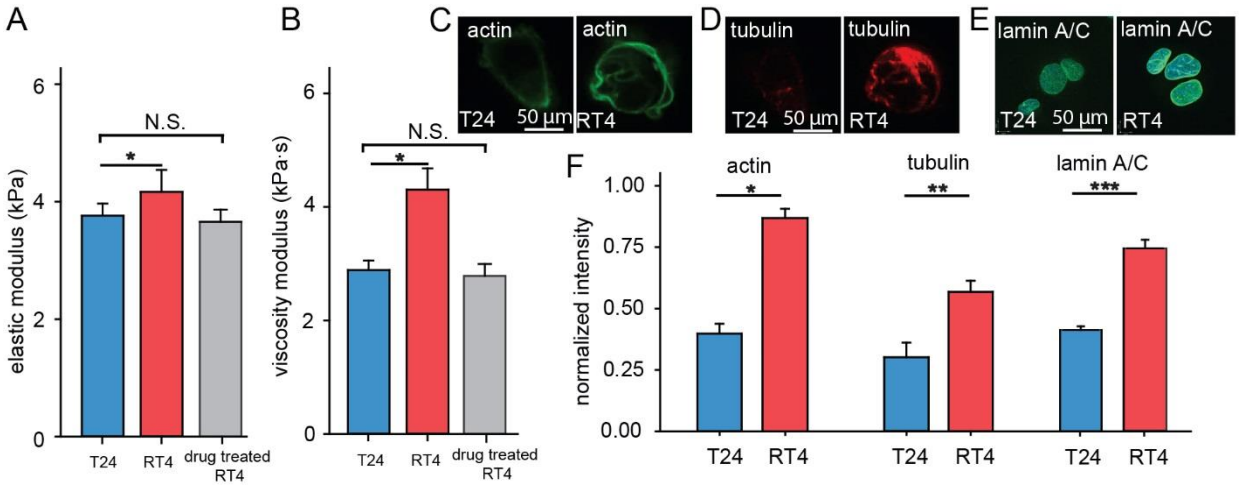

Figure 4. **Late-stage cancer cells possess a lower elastic modulus and viscosity.** Shown data were all measured on intact nuclei (i.e. not isolated). (A) Elastic modulus comparison between T24 and RT4 nuclei, mean±s.e.m., RT4 n = 24, T24 n = 31, $*P = 0.04$. (B) Viscosity comparison between T24 and RT4 nuclei, mean±s.e.m., RT4 n = 24, T24 n = 31, $*P = 3 \times 10^{-4}$. (C-F) Cytoskeleton difference and lamin differences. Chromatin intensity was used for normalizing the intensities. T24 express less tubulin, less actin, and less lamin than RT4. mean±s.e.m., RT4 n = 30, T24 n = 30, $*P = 3 \times 10^{-12}$, $**P = 3 \times 10^{-4}$, $***P = 3 \times 10^{-6}$.

Supplementary Materials

Table SI: comparisons of different methods used to characterize nuclear mechanics

Methods	Sample	Parameters	Advantages and Disadvantages	Example Results
micropipette aspiration	intact cell/ isolated nucleus	pressure, deformation	stiffness, viscosity, plasticity can be measured simultaneously; require isolation for cell nucleus	viscoelastic properties (Guilak et al. 2000) lamin networks (Harada et al. 2014)
AFM indentation and compression tests	isolated nucleus/ intact cell/ intact nucleus	force, indentation depth	fast, direct measurement, and various tip types offer more possibilities; large indentation causes nonlinearity of cell response.	cell characterization (Liu et al. 2014) isotropic cell nucleus (Haase et al. 2015)
microneedle manipulation	intact cell /intact nucleus	manipulated distance, deformation	lack precise estimation of force	nucleo-cytoskeleton coupling (Lombardi et al. 2011)
magnetic tweezers	intact cell /intact nucleus	force, deformation	force magnitude is highly controllable and the location force exerted on is precise; heat generation in workspace.	Mechanotransduction viscoelastic properties (Guilluy et al. 2014), cell plasticity (Bonakdar et al. 2016)
optical tweezers	intact cell /intact nucleus	force, deformation	force magnitude is highly controllable and the location force exerted on is precise; forces generated by optical tweezers are small.	chromatin, certain proteins in nuclear mechanics (Wang et al. 2009)
substrate strain test	intact cell	strain, deformation	convenient for observing cellular reactions by imaging; mechanical parameters are difficult to quantify.	nucleo-cytoskeleton coupling, substrate effects (Lombardi et al. 2011)
microfluidics	intact cell	deformation, channel/ pillar geometry etc.	stimulus is controllable; difficult to quantify mechanical parameters.	mechanical properties (Lammerding et al. 2006), substrate effects (Hanson et al. 2015)

Figure S1

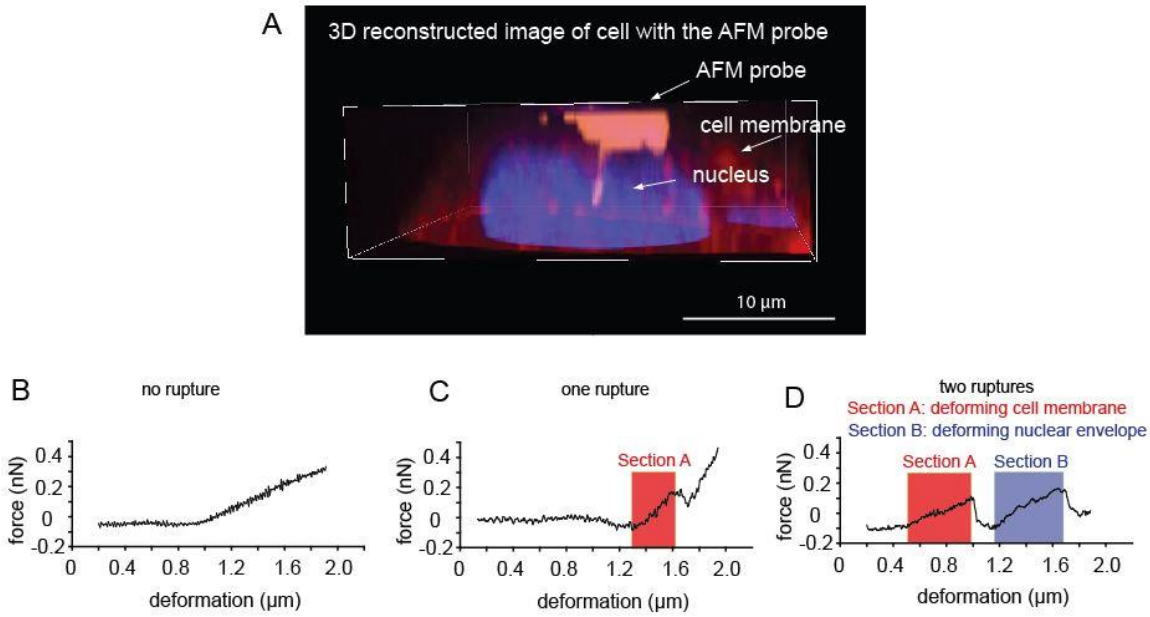

Figure S1. (A) 3D reconstructed image of a T24 cell whose membrane and nuclear envelope were both penetrated by the AFM probe. Blue: Hoechst, Red: CellMask Deep Red stain. (B-D) Representative experimental force-displacement curves. The force-displacement curves were collected through AFM indentation in the perpendicular direction. The data was used for analyzing the viscoelastic properties of the cell membrane, cytoskeleton, and nucleus. In-plane stress is difficult to extract from the measured results. (B) No rupture (indentation rate 1 µm/s). (C) One rupture (indentation rate 5 µm/s), and the nuclear envelope was not penetrated by the probe. (D) Two ruptures (indentation rate 10 µm/s). Only curves showing two clear ruptures were used for analysis. The probe first deforms and penetrates the cell membrane (Section A), then loads the cell nucleus until penetration of the nuclear envelope (Section B in Fig. 1(c)). The region between Section A and Section B is the probe traveling through the cytoplasm without indenting on a specific structure. Thus, data in this region was not fit into the contact mechanics model that was used for determining reduced modulus values in Section A and Section B. Data in this region contains the effect of the inhomogeneous distribution of cytoskeleton.

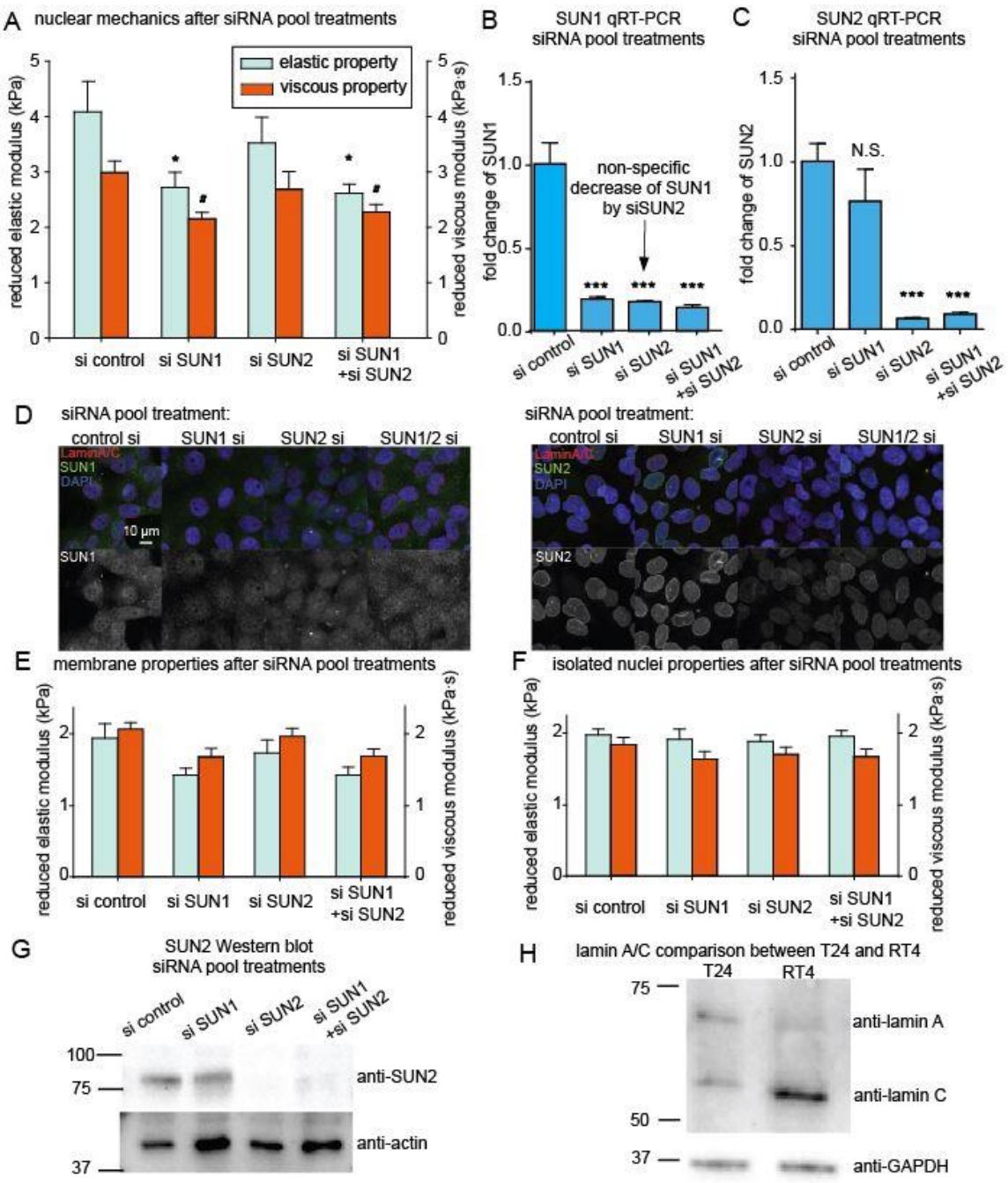

Figure S2. Nuclear mechanics after SUN protein knockdown using siRNA pool. (A) Reduced modulus and reduced viscosity of nuclei with SUN domain proteins knocked down by siRNA pool, mean±s.e.m., n = 15, *P < 0.02, #P < 0.005. (B) (C) qRT-PCR result for siRNA pool knockdown effects for SUN1 (B) and SUN2 (C), n = 4, ***P< 0.0001, N.S.: no significant difference. The results showed sufficient knock down of SUN1 and SUN2 proteins. It was also noticed that SUN2 siRNA pool induced significant non-specific decrease of SUN1 in (B). (D) SUN domain proteins knocked down using siRNA pool. The overall fluorescence intensity of the SUN1 protein significantly decreased after SUN1 siRNA pool treatment, compared with the group treated with the control siRNA. Similarly, the intensity of the SUN2 protein significantly decreased after SUN2 siRNA pool treatment, compared with the group treated with the control siRNA. (E) Reduced modulus and reduced viscosity of membrane with SUN 1/2 proteins knocked down by siRNA. Error bar: s.e.m., n = 15. No significance was observed between groups. (F) Reduced modulus and reduced viscosity of isolated nuclei with SUN 1/2 proteins knocked down by siRNA. No significance was observed between groups. Error bar: s.e.m., n = 15. (G) Western blot of SUN2 protein knockdown. T24 cells were treated with si control (10 nM), si SUN1 (10 nM), si SUN2 (10 nM) or si SUN1/2 (5 nM each = 10 nM total siRNA). Actin was used as control. (H) Western blot of lamin A/C comparison between T24 and RT4. GAPDH was used as control.

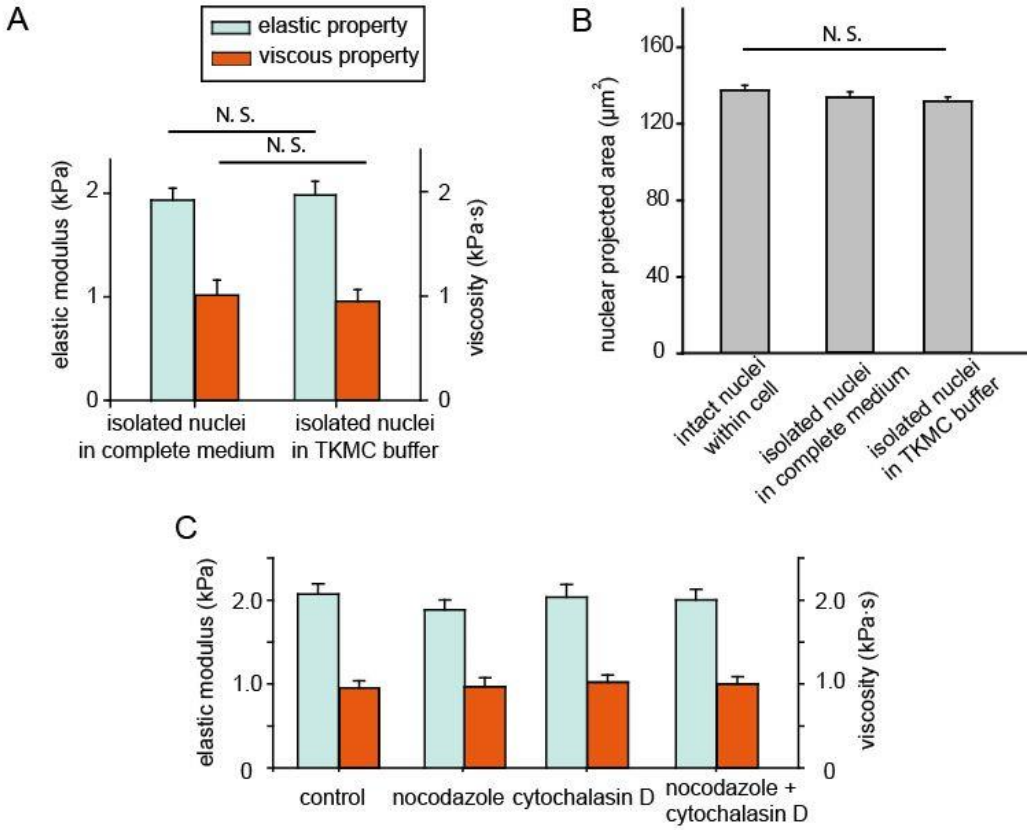

Figure S3. (A) Experimentally quantified elastic modulus and viscosity values of isolated nuclei in complete culture medium (McCoy's 5A Modified Medium) and in cell cytoplasm-mimicking TKMC buffer (50 mM Tris, pH 7.6, 25 mM KCl, 3 mM MgCl2, 3 mM CaCl2, 2 mg/ml each leupeptin and pepstatin). There was no significant difference observed between the measurements in complete culture medium and in the cytoplasm-mimicking buffer. Error bar: s.e.m., n= 15, *P= 0.85, **P= 0.73. (B) Nuclear projected area of intact nuclei within cell, isolated nuclei in complete cell medium, and isolated nuclei in TKMC buffer. The projected area of the isolated nuclei showed no difference between complete medium and the TKMC buffer. Error bar: s.e.m., n = 20, P= 0.5. (C) Anti-cytoskeleton drug treatments did not change the elastic modulus and viscosity of isolated nuclei. Error bar: s.e.m., n = 20, $P > 0.46$ for elastic modulus, and $P > 0.68$ for viscosity.